X-ray diffuse scattering associated with ferroelectric microregions in $KTa_{1-x}Nb_xO_3$

2001 J. Phys.: Condens. Matter 13 3257

(http://iopscience.iop.org/0953-8984/13/14/303)

INSTITUTE OF PHYSICS PUBLISHING JOURNAL OF PHYSICS: CONDENSED MATTER

J. Phys.: Condens. Matter **13** (2001) 3257–3270 www.iop.org/Journals/cm PII: S0953-8984(01)18250-0

X-ray diffuse scattering associated with ferroelectric microregions in $KTa_{1-x}Nb_xO_3$

H Abe[1,2], K Harada[3], R J Matsuo[3], H Uwe[3] and K Ohshima[3]

[1] Department of Materials Science and Engineering, National Defense Academy, 239-8686 Yokosuka, Japan
[2] Department of Physics, University of Houston, Houston, 77204-5506 TX, USA
[3] Institute of Materials Science, University of Tsukuba, Tsukuba 305-8573, Japan

Received 23 September 2000, in final form 23 January 2001

Abstract

X-ray diffuse scattering for single crystals of $KTa_{1-x}Nb_xO_3$ ($x = 0$, 0.007 and 0.011) has been measured. For the sample of $x = 0.011$, peculiar x-ray diffuse scattering is observed above the phonon-frozen-in temperature (30 K). By an analysis of the diffuse scattering intensities, the average radius of the ferroelectric microregions is found to grow up to around 4 nm with decreasing temperature from 100 K down to 30 K. Anisotropic distributions of the diffuse scattering indicate off-centred shift of Nb and Ta ions to the $\langle 111 \rangle$-direction. Moreover, lattice constants for $x = 0.011$ below 30 K exhibit negative expansion, which is found neither in pure $KTaO_3$ nor in $KTa_{1-x}Nb_xO_3$ ($x = 0.007$) at low temperatures. These results are successfully explained by introducing the effective classical potential (ECP) method for the anharmonic oscillators. The quantum contribution to mean square displacement of Nb and Ta ions from an average position is also calculated by the ECP method.

1. Introduction

It is well known that pure $KTaO_3$, whose structure is a simple cubic perovskite (space group $Pm3m$), shows characteristics of a typical quantum paraelectric. Recently, refinement of temperature dependence of the zone-centre soft-mode frequencies of $KTaO_3$ and $SrTiO_3$ was experimentally achieved by hyper-Raman scattering and theoretically performed by the method of effective classical potential (ECP) for linear-coupled anharmonic oscillators [1]. Ferroelectric transition is suppressed by quantum fluctuations, that is, zero-point motion at low temperature.

In nominally pure $KTaO_3$, Raman scattering from the soft-phonon branch in the Brillouin zone is induced by non-intentionally doped impurity [2, 3]. From observing an increasing scattering with lowering temperature, the origin is ascribed to the ferroelectric microregion (FMR), which centres at the impurity. The size of FMR changes from the order of the lattice constant, $a(T)$, at a high temperature to about $10a(T)$ at the lowest temperature. Here, the shape of the FMR was assumed as either a sphere [3] or an ellipsoid [2]. In an NMR experiment

0953-8984/01/143257+14$30.00

[4], it was found that the position of Nb impurities shifts from their cubic position below T_c in $KTa_{1-x}Nb_xO_3$ (KTN) ($x = 0.012$) and the host lattice forms the regions both of off-centred Ta and on-centred Ta. In $K_{1-x}Li_xTaO_3$ (KLT), a dipole is attributed to the off-centred position of Li near the ideal cubic K positions and its structure was calculated by a shell model [5].

In mixed crystals of KTN and KLT with the dilute contents, substitutional impurities play an important role in the structural behaviour relevant to soft phonon modes. Phase diagrams of KTN and KLT were reported in connection with quantum-ferroelectric and quantum-paraelectric phases [6, 7]. However, Gehring *et al* [8] did not find phase a transition in powdered crystals of KTN($x = 0.020$ and 0.030), though single crystals of KTN($x = 0.012$, 0.020 and 0.030) exhibited a ferroelectric phase transition ($T_{min} = 25$, 39 and 60 K). At the same time, these crystals showed negative thermal expansions at the low temperatures. The electric dipole glass has no long-range order (LRO) but short-range order (SRO) with the analogy of spin glass. In $KTa_{1-x}Nb_xO_3$ with $x = 0.008$, 0.012 and 0.02, Kleemann *et al* [9] have observed smeared phase transitions ($T_c = 10$ K, 17 K and 31.5 K) with LRO by refractive-index and linear-birefringence measurements. An idea of a 'cooperative dipole glass' has been introduced to explain their results; clusters, which have SRO, interact with each other. The cooperative dipole glass seems to be similar to the recently discussed relaxor [10] such as $PbMg_{1/3}Nb_{2/3}O_3$ and $PbSc_{1/2}Ta_{2/3}O_3$ with respect to dielectric properties. Here, the relaxors are related with charge ordering, though KLT and KTN are not.

A neutron inelastic scattering experiment in KTN($x = 0.012$) was carried out to clarify the relationship between the dipole glass transition and phonon softening [11, 12]. As the result, the incomplete softening at the zone-centre TO mode [11] was observed at 20 K, whose result coincides with the results by light scattering; both results show the minimum frequency at 20 K. Moreover, the TA phonon mode [12] was investigated in KTN($x = 0.00$, 0.012 and 0.03). In particular, the mode in KTN($x = 0.012$) has smallest frequency at 20 K and is strongly coupled with the TO mode. TA phonon mode is the lowest mode in all branches and couples with TO mode near the zone centre [13, 14]. Further, Andrews [15] observed an abnormal x-ray diffuse scattering both from KTN and KLT under zero electric field or non-zero electric field, whose diffuse scattering appears close to Bragg reflections.

In this study, we have measured x-ray diffuse scattering for single crystals of KTN to investigate the shape and size of FMR and also obtained an x-ray diffraction pattern to determine to the temperature dependence of the lattice parameter.

2. Theory

2.1. The effective classical potential method

The mean square displacements are calculated by using the effective classical potential (ECP) method [1]. We employ the ECP, $V(u)$, for the off-centred Nb and Ta ion motion as follows,

$$V(u) = \tfrac{1}{2}M\omega_1^2u^2 + \lambda u^4 + \mu u^6 \qquad (\mu > 0) \tag{1}$$

where u is the atomic displacement from an average position, ω_1 is the oscillator frequency in the harmonic limit and M is an appropriate mass. λ and μ indicate quartic and sextic anharmonicity coefficients, respectively. For simplicity, energies, temperatures and lengths are normalized by $\hbar\omega_1$, T_1 and $(\hbar/M\omega_1)^{1/2}$, respectively ($T_1 = \hbar\omega_1/k_B$), where k_B is the Boltzmann constant. Then, equation (1) becomes

$$V(u) = \frac{1}{2}u^2 + \tilde{\lambda}u^4 + \tilde{\mu}u^6 \qquad \tilde{\lambda} = \lambda\frac{\hbar\omega_1}{(M\omega_1^2)^2} \qquad \tilde{\mu} = \mu\frac{(\hbar\omega_1)^2}{(M\omega_1^2)^3} \qquad (\tilde{\mu} > 0). \tag{2}$$

Using this potential, the mean square displacement from an average position, $\langle u^2\rangle_{ECP}$, is given by

$$\langle u^2(T)\rangle_{ECP} = \langle \zeta^2(T)\rangle + \langle a^2(T,\zeta)\rangle \tag{3}$$

where ζ is the 'classical' displacement coordinate and $a^2(T,\zeta)$ is the quantum contribution to the mean square displacement for the anharmonic oscillator. ζ is defined as the average value of u. The model calculation is performed as the average of $V(u)$ over a Gaussian displacement distribution at the centre of the 'classical' position ζ. $a^2(T,\zeta)$ is derived from the self-consistent calculation and is described in appendix B of [1].

2.2. Thermal diffuse scattering

For simplicity, we introduce $\boldsymbol{q}$ as $\boldsymbol{q} = \boldsymbol{K} - \boldsymbol{G}_{hkl}$, where $\boldsymbol{K}$ is the scattering vector and $\boldsymbol{G}_{hkl}$ is the reciprocal lattice vector for the (hkl) plane. Due to the elastic wave of wavevector $\boldsymbol{q}$ and vibration direction $\boldsymbol{e}_j$ $(j = 1, 2, 3)$, the displacement of atom n can be expressed by

$$\boldsymbol{u}_n(qj) = a_{qj}\boldsymbol{e}_{qj}\exp\{\mathrm{i}(\boldsymbol{K}\cdot\boldsymbol{r}_n - \omega_{qj}t)\}. \tag{4}$$

Using the average energy associated with the wave qj, $\langle E_{qj}\rangle$, the first-order thermal diffuse scattering (TDS) is described as [16]

$$I_1(K) = \frac{|F|^2}{V_c m}\sum_j \frac{(K e_{qj})^2\langle E_{qj}\rangle}{\omega_{qj}^2} \qquad \frac{\langle E_{qj}\rangle}{\omega_{qj}^2} \propto \langle a_{qj}^2\rangle \tag{5}$$

where F is the structure factor containing the temperature factor, V_c is the volume of the unit cell. Furthermore, we calculate the advanced TDS intensities by Wooster's method [17]. This equation is written as

$$I^{TDS}(q,T) = \frac{|F|^2}{V_c}\left(\frac{K}{q}\right)^2\sum_{i,j,l}\hat{h}_i\hat{h}_j(A^{-1})_{ij}\langle E_{ql}\rangle \qquad \hat{h} = G_{hkl}/|\boldsymbol{G}_{hkl}| \tag{6}$$

A_{ij} consists of $\hat{q} = q/|\boldsymbol{q}|$ and elastic constants, C_{11}, C_{12} and C_{44} for cubic crystals. Here, elastic anisotropy is expressed by A_{ij}, that is, the gradient at $q = 0$ of phonon dispersion curve.

2.3. Huang diffuse scattering

According to Huang diffuse scattering (HDS) theory [18], $I^{HDS}(\boldsymbol{q})$ is connected with the symmetry of static dilute defects. This symmetry is described by a dipole tensor, P_{ij}. For instance, P_{ij} in equation (7) reveal a [111]-dipole tensor. Note that $I^{HDS}(\boldsymbol{q})$ is not derived from defects themselves, but from the distorted region around them. Since the strain is spread over the whole crystal in real space, HDS appears around the zone centre in the reciprocal lattice. Generally, we can ignore the scattering from defect themselves due to low impurity concentration. If defect concentration increases and one defect has a correlation with others, the modulations of diffuse scattering are observed along various directions. $I^{HDS}(\boldsymbol{q})$ is provided by

$$I^{HDS}(q) = c|F|^2\left(\frac{G_{hkl}}{q}\right)^2\left|\frac{1}{V_c}\sum_{i,j,l}\hat{h}_i g_{ij}(\hat{q})\hat{q}_l P_{jl}\right|^2 \qquad P_{ij} = \begin{pmatrix} P_{11} & P_{12} & P_{12} \\ P_{12} & P_{11} & P_{12} \\ P_{12} & P_{12} & P_{11}\end{pmatrix}. \tag{7}$$

$g_{ij}(\hat{q})$ is a function of elastic constants, C_{11}, C_{12} and C_{44} for cubic crystals. c is the concentration of defects. In the cluster of defects, $I^{HDS}(\boldsymbol{q},T)$ is proportional to the number of defects within one cluster. In addition, these local defects have a relation with lattice constants as a macroscopic property. For instance, interstitial impurities cause the lattice expansion.

On the other hand, atomic vacancies cause the negative lattice expansion. The lattice change is calculated as

$$\frac{\Delta V}{V} = 3\frac{\Delta a}{a} = \frac{c\sum_i P_{ii}}{V_c(C_{11} + 2C_{12})} \tag{8}$$

for cubic crystals.

3. Experiment

Single crystals of $KTa_{1-x}Nb_xO_3$ were prepared with the use of the top-seeded solution growth method at the University of Tsukuba. We have used four single crystals, with Nb compositions, x, of 0.000, 0.007, 0.011 and 0.025, whose sizes are $6.4 \times 6.0 \times 1.5$ mm^3, $4.3 \times 3.2 \times 2.4$ mm^3, $3.4 \times 3.1 \times 2.4$ mm^3 and $9.3 \times 7.2 \times 4.6$ mm^3, respectively. The faces of the specimens are perpendicular to $\langle 100 \rangle$ directions. The Nb composition was determined by the electron-probe microanalysis. First, we have performed experiments on temperature dependence of lattice constants for the specimens by x-ray diffraction methods with the use of reflection geometry, where KTN($x = 0.025$) was measured only at room temperature. Cu K$\bar{\alpha}$ radiation was used as the primary beam. Highly oriented pyrolytic graphite (002) was used to obtain a monochromated beam, whose wavelength, λ, is 0.154 18 nm. Lattice constants were estimated from the position of Bragg peaks in a range from room temperature to 16 K on a low-temperature four-circle diffractometer at the University of Tsukuba. The cryostat, mounted on a Huber Eulerian cradle (model 512), was a closed-cycle cryogenic refrigerator manufactured by Air Products (model DE202). As diffuse scattering deriving from defects appears near Bragg reflections, we needed high-resolution x-ray experiments to reduce the intensities from the tail of Bragg reflections. Hence, we have performed the measurement to take the temperature dependence of diffuse scattering on a Huber 5020.4 four-circle diffractometer installed at BL-4C at the Photon Factory of the High Energy Accelerator Research Organization. The curved mirror was placed before a Si(111) double monochromator to obtain a stronger primary beam, whose wavelength was 0.1542 nm. The cryostat was the same type as that at the University of Tsukuba. The mosaic spread of KTN($x = 0.011$) was 0.0348 (nm^{-1}), where the full width at half maximum (FWHM) at BL-4C for the incident beam was found to be 0.0057 (nm^{-1}). The temperature of the sample was stabilized within ± 0.05 K.

4. Experimental results and analysis

Lattice constants of KTN($x = 0.000$, 0.007, 0.011 and 0.025) have composition dependence at room temperature as shown in figure 1, where the lattice constant increases slightly with increasing Nb concentration. Figure 2(a) shows the temperature dependence of lattice constants for the three specimens ($x = 0.00$, 0.007 and 0.011). Each lattice constant was obtained by the average of plus 2θ and minus 2θ values for the coupled Bragg reflections. This method can compensate for the errors of sample centring or beam centring. For $x = 0.011$, we find negative thermal expansion below 30 K, though the normal behaviour of temperature dependence of the lattice constants appears for $x = 0.000$ and 0.007.

On the other hand, integrated intensity $I(T)$ is connected with lattice constant $a(T)$ and the isotropic temperature factor $B(T)$ ($= 8\pi^2\langle u^2 \rangle$) as follows:

$$\frac{I(T)}{I(0)} = \exp\left\{ -2B(T)\left(\frac{\sin\theta}{\lambda}\right)^2 \right\} = \exp\left\{ -B(T)\frac{h^2 + k^2 + l^2}{2\{a(T)\}^2} \right\}. \tag{9}$$

Temperature dependences of the average integrated intensity in several Bragg reflections were obtained in pure $KTaO_3$, KTN($x = 0.007$) and KTN($x = 0.011$), respectively. By using

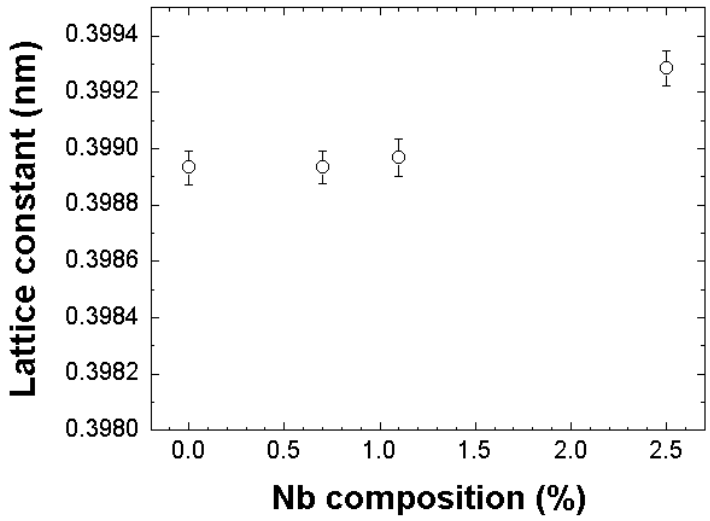

Figure 1. Lattice constants of $KTa_{1-x}Nb_xO_3$ as a function of Nb composition at room temperature.

Table 1. Nb concentration dependence of T_1, $\tilde{\lambda}$ and $\tilde{\mu}$ of $\langle u^2 \rangle_{ECP}$. These parameters are determined by self-consistent calculations using ECP method (see text). Those for pure $KTaO_3$ ($x = 0.000$) refer to [1].

x	T_1 (K)	$\tilde{\lambda}$	$\tilde{\mu}$
0.000	(53)	(0.6)	(0.0)
0.007	110	0.58	0.00
0.011	225	0.53	0.00

equation (9), the isotropic temperature factor was obtained from the observed integrated intensities and the lattice parameter as shown in figure 2(b). The temperature factor is linear with temperature at high temperatures, but is almost constant below 100 K. This can be attributed to the quantum effect of the zero-point atomic motion. Solid curves in figure 2(b) are calculated by the following procedure. We invoke the dominant fluctuation of the atomic displacement as that of the ferroelectric soft TO [100] mode. This is because the frequency for the soft TO phonon is nearly equal to that of acoustic phonon. Considering the only TA phonon mode, we calculate the mean square displacement, $\langle u^2(T) \rangle_{ECP}$, using equations (1)–(3). This $\langle u^2(T) \rangle_{ECP}$ is connected with the lattice constant in equation (9). $a^2(T, \varsigma)$ is effective at low temperature by the influence of anharmonic displacements relating to the precursor phenomenon of the phase transition. Comparing $\langle u^2 \rangle_{ECP}$ with $\langle u^2 \rangle_{obs}$, parameters T_1, $\tilde{\lambda}$ and $\tilde{\mu}$ are determined self-consistently. The actual best-fitted parameters, T_1, $\tilde{\lambda}$ and $\tilde{\mu}$ of $\langle u^2 \rangle_{ECP}$ are shown in table 1, where we refer to Vogt's results for pure $KTaO_3$ [1]. Solid curves in figure 2(b) are those fitted by the ECP method. We find that T_1 increases with Nb content, while $\tilde{\lambda}$ is essentially constant. Decreasing mass value from Ta to Nb seems to affect the increasing frequency. Finally, the solid curves in figure 2(a) are derived from $B_{ECP}(T, T_1, \tilde{\lambda}, \tilde{\mu})$ and a polynomial fit of the observed integrated intensity.

Figure 3 shows the temperature dependence of the full width at half maximum (FWHM) of KTN($x = 0.011$) for a radial scan of the 002 Bragg reflection, where data were obtained at the Photon Factory of the High Energy Accelerator Research Organization. We refer to the temperature dependence of the lattice constant of KTN($x = 0.011$) in order to emphasize

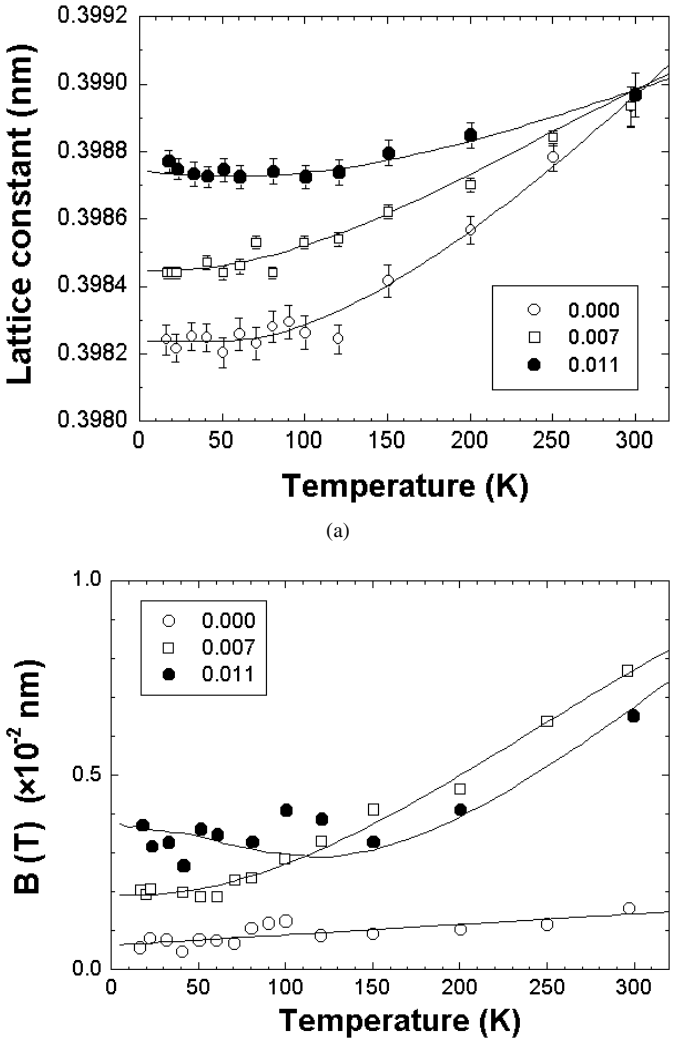

Figure 2. (a) Lattice constants of $KTa_{1-x}Nb_xO_3$ as a function of temperature. Open circles, open squares and solid circles correspond to $x = 0.000$, $x = 0.007$ and $x = 0.011$, respectively. Each solid line is calculated by using the effective classical potential (ECP) method (see text), where only a solid curve in pure $KTaO_3$ is calculated using parameters in a previous paper [1]. (b) The temperature dependence of the isotropic temperature factor, $B(T)$. Open circles, open squares and solid circles correspond to $x = 0.000$, $x = 0.007$ and $x = 0.011$, respectively. $B(T)$ is determined by the temperature dependence of both integrated intensities and lattice constants. Solid curves are calculated by using the ECP method.

the negative thermal expansion below 30 K. The value of FWHM increases below 30 K, where the negative thermal expansion is seen. The increase of FWHM was also seen in the 103 Bragg reflection. These increases of FWHM agree with previous results [12], where the lattice constant of KTN($x = 0.012$) has a minimum value at 20 K (T_{min}). Furthermore, both TO and TA phonon modes are reported to have the minimum energy at T_{min}. On the other hand, we find that the FWHM of the 202 Bragg reflection has no increase below 30 K.

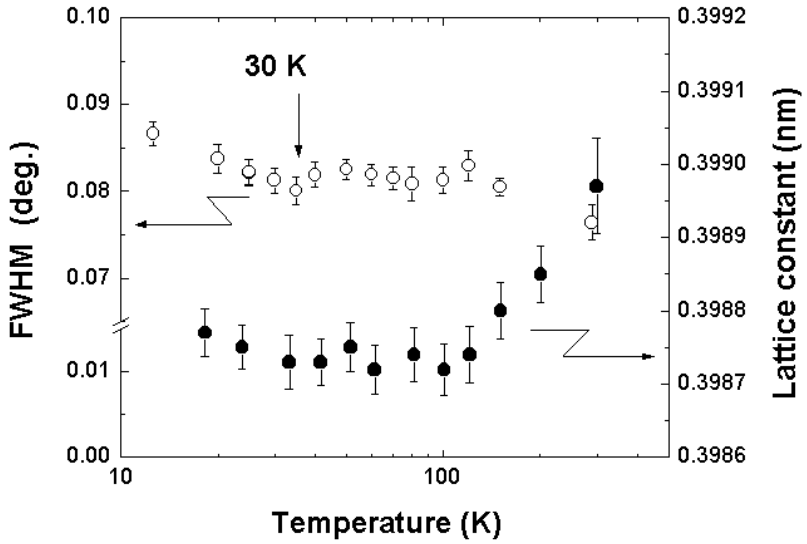

Figure 3. Temperature dependence of the full width at half maximum (FWHM) of the 002 Bragg reflection along the radial direction in $KTa_{1-x}Nb_xO_3$ ($x = 0.011$) (open circles). FWHM also increases below 30 K. To emphasize the anomaly below 30 K, lattice constants (closed circles) are also seen.

In KTN($x = 0.011$), the observed diffuse intensities are provided as $I^{diff}(\boldsymbol{q}, T) = I^{TDS}(\boldsymbol{q}, T) + I^{HDS}(\boldsymbol{q}, T) + I^{BG}(\boldsymbol{q})$, where $I^{BG}(\boldsymbol{q})$ represents the intensity of the background (BG). We estimate the background using an Si single crystal. Equation (6) represents the contributions of various TA phonon modes around the zone centre, because the TA phonon mode is coupled with TO phonon softening around the zone centre. Here, the temperature dependence of elastic constants in pure $KTaO_3$ [19, 20] is included in $(A^{-1})_{ij}$ in equation (6). Here, we analyse the observed diffuse scattering intensity: the calculated $\langle u^2(T)\rangle_{ECP}$ is proportional to $\langle E_{qj}\rangle$ in equation (5). Using the temperature dependence of diffuse scattering above 100 K, we scaled the calculated intensity into the observed one. This is because additional diffuse scattering appears below 100 K. In figure 4, the temperature dependence of diffuse scattering intensity at $\xi = 0.629$ along the $\boldsymbol{G}_{002} + \boldsymbol{q}[\xi 00]$ direction in $KTa_{1-x}Nb_xO_3$ ($x = 0.011$) was depicted, where the reciprocal lattice unit (r.l.u.) is used to present the q value. In the figure, we have averaged diffuse scattering intensities to ignore the asymmetric part due to size effect modulation. Symmetric diffuse intensities, $S(\boldsymbol{q}, T)$, were estimated as $\{I^{diff}(\boldsymbol{q}, T) + I^{diff}(-\boldsymbol{q}, T)\}/2$. A broken curve is quite different from the observed values below 100 K. Thus, we assume the following concept to interpret the above discrepancy. Raman scattering experiment revealed that FMR grows below 100 K with accompanying phonon softening [2, 3]. Here, the components of FMR are an off-centred Nb ion at the centre of FMR and an off-centred Ta ion surrounding it. Since Nb ions are substituted for Ta ones randomly, FMR appears below 100 K independently. The increase of the diffuse scattering intensity below 100 K can be attributed to the increase of the size of FMR. Diffuse scattering intensities are, however, decreasing below 30 K. Considering the lattice expansion below 30 K as shown in figure 3, we judge that further growth of FMR due to its cooperate interaction with each other expands to the whole crystal. Here, FMR with large volume leads to the diffuse scattering with a smaller q region. Thus, diffuse scattering intensities within the observed q region decrease below 30 K.

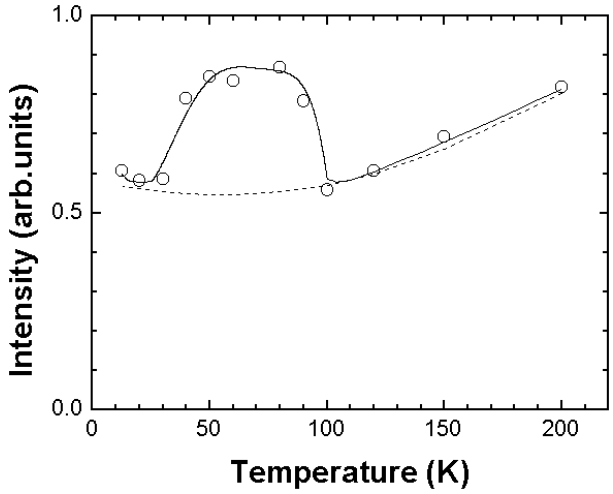

Figure 4. Temperature dependence of diffuse scattering at $\xi = 0.629$ along the $\boldsymbol{G}_{002} + \boldsymbol{q}[\xi 00]$ direction in $KTa_{1-x}Nb_xO_3$ ($x = 0.011$), where the unit of q is the reciprocal lattice one. A solid line shows the summation of the calculated thermal diffuse scattering and Huang diffuse scattering, while a broken line shows the calculated thermal diffuse scattering.

We propose the following model in order to analyse experimental results based on the above concept. The displacement direction of off-centred both Nb and Ta ions in FMR is the [111]-direction. Because the soft phonon mode of TA[100] is coupled with other equivalent TA[010] and TA[001] phonon modes near the zone centre below 100 K, three phonon modes become the TA[111] mode and cause the [111]-displacements. The [111]-displacement at low temperatures is expected from the phase diagram of $KTaO_3$–$KNbO_3$, because the lowest-temperature phase has rhombohedral symmetry [21]. Moreover, Eglitis *et al* [22] suggested that the direction of off-centred Nb ion prefers the [111]-direction to [100]. We apply this idea to the isolated FMR. In this case, an expression for concentration of total dipoles, c in equation (8), is rewritten as xN_{cl} ($x = 0.011$), where N_{cl} is the number of off-centred dipoles within one FMR. Therefore, equation (8) is modified as follows:

$$3\frac{\Delta a}{a} = \frac{xN_{cl}\sum_i P_{ii}}{V_c(C_{11} + 2C_{12})}. \tag{10}$$

The actual magnitude of dipoles within FMR decreases with increasing distance from the centre of FMR. However, we consider uniform dipoles within FMR and ignore the size distribution of FMR. Thus, an actual average size of FMR is estimated to be larger than the calculated one. Next, we assume that the shape of FMR is spherical for simplicity. N_{cl} has a relation with the radius, R_{cl}, of a spherical FMR and is described as

$$N_{cl}V_c = (4\pi/3)R_{cl}^3. \tag{11}$$

$P_{ij}(T)$ in equation (7) is the dipole tensor of the defects along the [111]-direction. The temperature dependence of $P_{11}(T)$ is determined by equation (8) with the lattice constant. In HDS theory, local defects provide the long-range strain over the whole crystal elastically. This strain has an influence on the lattice constant as the macroscopic property. The origin of diffuse scattering from defects is not a part of the local strains generated by defects themselves, but long-range strains. Hence, inhomogeneous strains are connected with the lattice constant by equation (8). On the other hand, $R_{cl}(T)$ and $P_{12}(T)$ are unknown. The HDS

intensity depends both on the concentration term, $xN_{cl}(T)$, and the $P_{ij}(T)$ term. Though both terms have the relation with $R_{cl}(T)$ in equations (10) and (11), they are of the opposite property. $N_{cl}(T)$ is proportional to $\{R_{cl}(T)\}^3$, but $P_{ij}(T)$ is nearly inversely proportional to $N_{cl}(T)$ by equation (8). This competition between $N_{cl}(T)$ and $P_{ij}(T)$ makes it difficult to calculate HDS intensities. Therefore, we introduce the self-consistent calculations by Monte Carlo methods to determine $R_{cl}(T)$. The judgement of the Monte Carlo calculation is obtained by the convergence of weighted reliability factor, wR, since HDS intensities is stored from 10 to 10 000 counts: wR is $(= \sqrt{\sum w|I^{obs} - I^{cal}|^2 / \sum w|I^{obs}|^2})$, where $I^{cal} = N_{cl}(T)I^{HDS}(\boldsymbol{q}, T)$, $I^{obs} = S(\boldsymbol{q}, T) - I^{TDS}(\boldsymbol{q}, T) - I^{BG}(\boldsymbol{q})$ and $w = 1/I^{obs}$. Elastic constants, C_{11}, C_{12} and C_{44} in equation (7) are the same value as used in the TDS calculation.

As the result, $R_{cl}(T)$ values in various directions are calculated as shown in figure 5. The derived value of the FMR size below 100 K at each direction is found to be around 4 nm. It is considered that we succeed to remove TDS from the total diffuse intensity, because the above calculation results of FMR size provide almost the same order among different three directions; these are the L (longitudinal) direction of 002 and both L and T (transverse) directions of the 103 Bragg reflection. In the other three directions which are 002 (T direction) and 202 (T and L directions), the self-consistent $R_{cl}(T)$ calculations have no coincidence with experimental results. The reason is why the calculated HDS intensities become zero or so small compared with the calculated TDS intensities. In detail, we discuss the anisotropic distributions of HDS later. While, the observed diffuse intensity is decreasing below 30 K as shown in figure 5. We interpret that the decrease of the calculated size of FMR below 30 K is caused by experimental restriction of q region. The actual size of FMR is probably increasing continuously below 100 K. The previous study shows continuous growth of FMR below 100 K [2, 3]. This proves that the method of above calculation and the assumption are accurate. A solid line in figure 4 shows the calculated intensity of the total diffuse scattering at $\boldsymbol{G}_{002} + \boldsymbol{q}[\xi 00]$ ($\xi = 0.629$) using the calculated $R_{cl}(T)$.

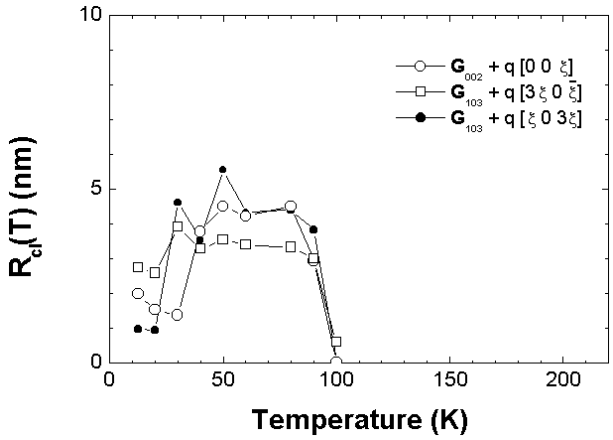

Figure 5. Temperature dependence of the calculated radius of FMR cluster, R_{cl}. R_{cl} values along various directions are analyzed by the self-consistent Monte Carlo method using the observed diffuse scattering.

The next step is to investigate both $\boldsymbol{q}$ and temperature dependences of diffuse scattering at various directions. Figure 6(a) shows the temperature dependence of the observed diffuse scattering intensity at $\boldsymbol{G}_{002}$ + $\boldsymbol{q}[\xi 00]$, where each line designates the intensity contour. Figure 6(b) shows the temperature dependence of the calculated one at the same direction.

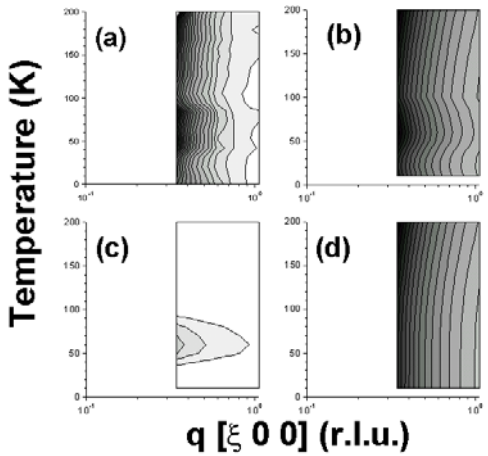

Figure 6. Temperature dependence of (a) the observed diffuse scattering, (b) the calculated one, (c) the calculated Huang diffuse scattering (HDS) and (d) the calculated thermal diffuse scattering (TDS) along $\boldsymbol{G}_{002} + \boldsymbol{q}[\xi 00]$ in $KTa_{1-x}Nb_xO_3$ ($x = 0.011$).

Figure 6(b) can be divided into two contributions; one is HDS as seen in figure 6(c) and the other is TDS as seen in figure 6(d). The calculated HDS intensity has a coincidence with the observed one. To clarify the direction dependence of diffuse scattering, we show the normalized diffuse scattering intensities, $S(\boldsymbol{q})$, at 60 K along the various directions as shown in figure 7. $S(\boldsymbol{q})$ is given by

$$S(\boldsymbol{q}, 60\ \mathrm{K}) = \{I^{diff}(\boldsymbol{q}, 60\ \mathrm{K}) - I^{BG}(\boldsymbol{q})\}/|\bar{f}|^2 \qquad \bar{f} = f_K + (1-x)f_{Ta} + xf_{Nb} + 3f_O \tag{12}$$

where f_K, f_{Ta}, f_{Nb} and f_O are the atomic scattering factors of K, Ta, Nb and O ions, respectively. Note that both HDS and TDS intensities are proportional to $|\boldsymbol{G}_{hkl}|^2$ in equations (6) and (7). In fact, $S(q)$ along G_{103} (T and L direction) are larger than those along G_{002}. However, the above relationship cannot be satisfied in $S(q)$ around 002 and 202 Bragg reflections. Along T direction, $S(q)$ around the 202 Bragg reflection is much smaller than that around the 002 one, though $|\boldsymbol{G}_{202}|^2$ is greater than $|\boldsymbol{G}_{002}|^2$. This remarkable difference of $S(q)$ between 202 and 002 results in the FMR symmetry, where both HDS and TDS contributions must be considered at this temperature. In general, the anisotropic distributions of TDS are caused by the anisotropy of elastic constant. On the other hand, HDS depends on q directions by both FMR symmetry and elastic anisotropy.

Further, an analysis of diffuse intensities at different directions makes clear the [111]-displacement of off-centred Nb and Ta. In particular, the anisotropic distributions of diffuse scattering around the 202 Bragg reflection are the key to resolving FMR symmetry. In fact, the calculation of HDS with the [111]-displacements of Nb and Ta ions is the most appropriate distribution among [100]-, [110]- and [111]-displacement models as shown in figures 8(a), 8(b) and 8(c), respectively. The calculated HDS with [111]-displacement at $\boldsymbol{G}_{202}$ (T direction) becomes 0 due to FMR symmetry by HDS theory, as shown in figure 8(c). On the other hand, the calculated ones with [100]- or [110]-displacement in the same direction are nearly three times larger than those at $\boldsymbol{G}_{202}$ (L direction). We conclude that the direction of off-centred Nb and Ta is the [111]-direction by the above analysis. In addition, very weak diffuse scattering at $\boldsymbol{G}_{202}$ (T direction) suggests their actual displacements are not the exact [111]-direction. The dipoles along the [111]-direction have random and small rotational fluctuations along the

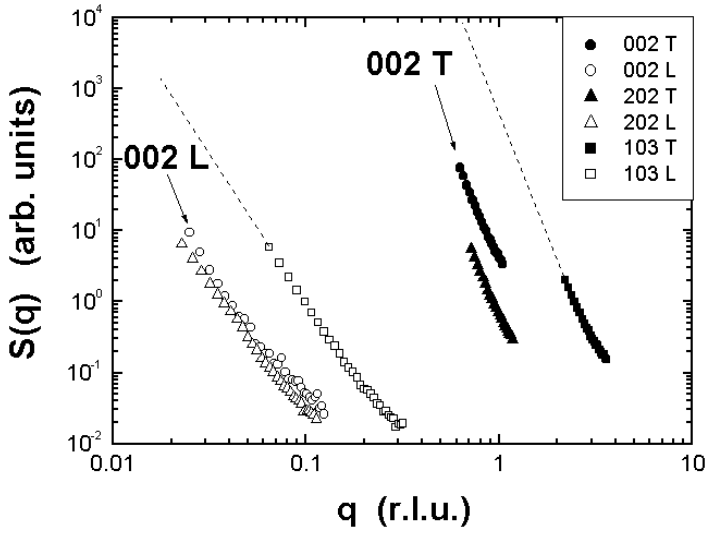

Figure 7. Temperature dependence of the observed diffuse scattering at 60 K along transverse and longitudinal directions around 002, 202 and 103 Bragg reflections.

[111]-directions, while we calculate the TDS distribution around the 202 Bragg reflection for comparison (figure 8(d)). In this case, the anisotropic distribution of TDS is derived from TA[100] phonon softening.

There is another method to determine the size of FMR. Diffuse intensity exhibits both q^{-2} and q^{-4} dependences if distinct clusters of defects are generated, as shown in figure 9. HDS theory [18] exhibits that the crossover point, q_c, from the q^{-2} to q^{-4} dependences, provides an average cluster size. As a result, FMR size is estimated to be 10 nm by q_c along $G_{002} + q[00\xi]$ at 60 K from figure 9. R_{cl} is estimated to be 4 nm in figure 5. The estimation of FMR size from q_c is comparable to that from R_{cl}, since the diameter of the spherical FMR becomes 8 nm.

5. Remarks

At first, we discuss the relation between anharmonic quantum fluctuations in the ECP method and lattice constants. In the ECP method, $\langle u^2 \rangle$ is divided into the classic harmonic fluctuations, $\langle \xi^2 \rangle$, and anharmonic quantum fluctuations, $\langle a^2 \rangle$. When temperature is smaller than T_1, $\langle a^2 \rangle$ is much more effective than $\langle \xi^2 \rangle$. This is because T_1 is defined by the oscillator frequency in the harmonic limit, while T_1 is nearly proportional to Nb concentration. In this system, the competition between long-range elasticity and glasslike freezing is not so trivial against Nb composition. Certainly, Nb concentration is an also order parameter of the phase transition in previous studies [6]. Note that the specific soft mode is not determined by this one-dimensional model using $\langle a^2 \rangle$, though these anharmonic fluctuations have some relation with phonon softening at low temperature.

Next, we summarize the appearance and development of FMR. The occurrence and development of FMR is explained by previous and present results. We distinguish the correlated FMR below 30 K from the small isolated FMR between 100 and 30 K. FMR is formed independently at the centre of Nb impurities. Nb impurities are replaced at Ta positions randomly. Below 100 K, Nb impurities shift to off-centred positions. At the same time, Ta ions around Nb ions also shift to the off-centred position along the same direction. By observing

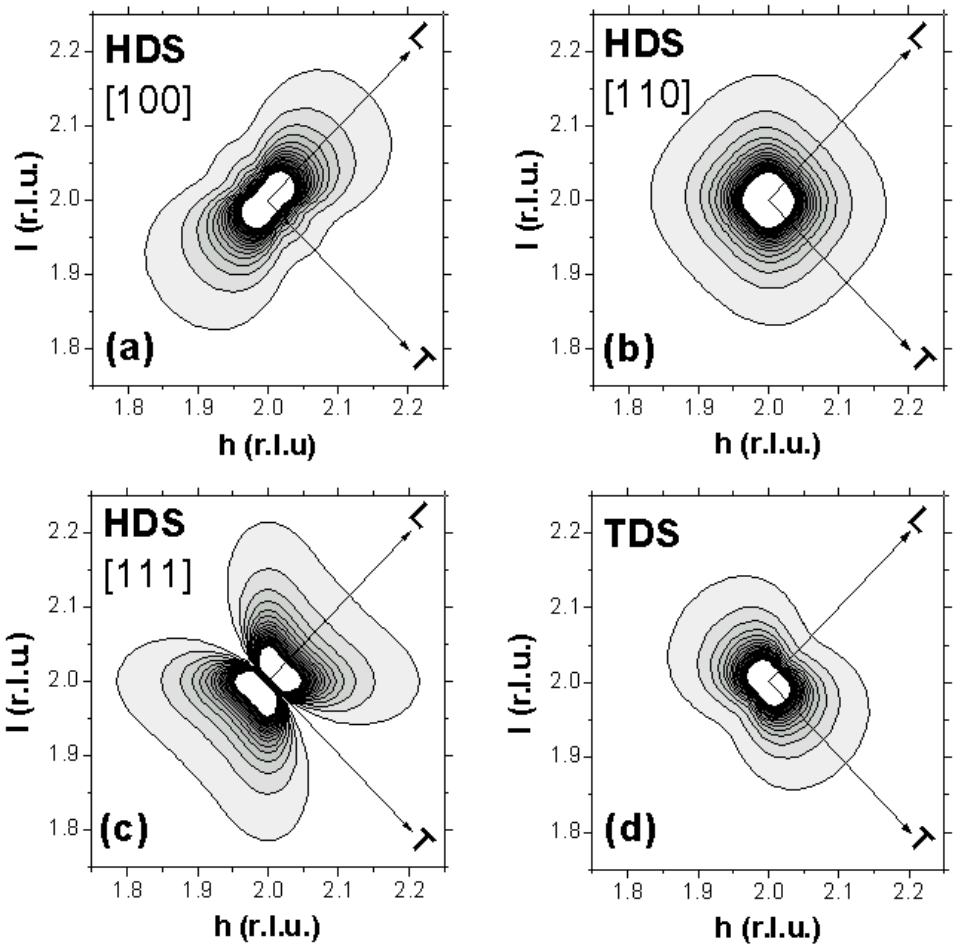

Figure 8. The calculated distributions of Huang diffuse scattering around the 202 Bragg reflection using the shift of off-centred Nb, whose direction is (a) the [100]-direction, (b) the [110]-direction and (c) the [111]-direction. (d) For comparison, the calculated distribution of thermal diffuse scattering around the 202 Bragg reflection is also shown.

the distinct anisotropic distributions of HDS only around G_{202}, we have determined that the possible off-centred direction is the ⟨111⟩-direction among the ⟨100⟩-, ⟨110⟩- and ⟨111⟩-directions. Compared with the simulation of HDS with experimental results, some rotational fluctuations, which are random and small, are suggested along the ⟨111⟩-direction. The size of FMR becomes larger with decreasing temperature with the help of phonon softening. We estimate the size of FMR at around 10 nm by the q dependence of the HDS intensity. The increase of diffuse intensities from 100 to 30 K reflects the developments of isolated FMR.

Below 30 K, each FMR has a correlation and strong strains appear over a whole crystal. This tendency has concurrence with the increases of the lattice constant and of FWHM of KTN($x = 0.011$) below 30 K, since long-range strains contribute to FWHM or to the lattice constant as a macroscopic property. The correlated FMR develops cooperatively with increasing size to contact with neighbouring FMR with different polarization directions. Since it is difficult to consider that FMR disappears below 30 K suddenly, the reasons for decrease

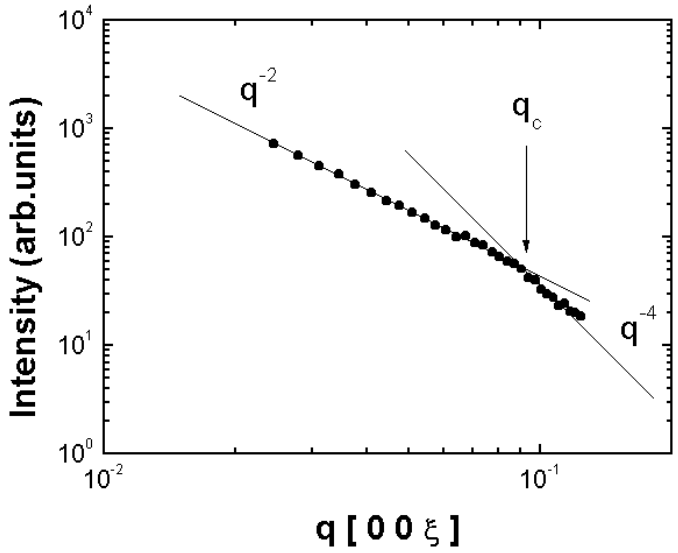

Figure 9. q dependence of Huang diffuse scattering along the $\boldsymbol{G}_{002} + \boldsymbol{q}[00\xi]$ at 60 K. A crossover point, q_c, between q^{-2} and q^{-4}, can provide the average size of FMR. It is estimated to be around 10 nm.

of HDS intensity in this temperature region are the measurement restrictions of the q region. Hence, the decrease of HDS means that HDS intensity along various directions shifts to a smaller q region.

Lattice constants of pure $KTaO_3$ decrease monotonically with decreasing temperature. Furthermore, the temperature change of lattice constants in KTN($x = 0.007$) is smaller than that in pure $KTaO_3$ over the temperature range between room temperature and 16 K. Their monotonic decrease is also seen in KTN($x = 0.007$) with decreasing temperature. We expect that the existence of FMR has great influence on not only absolute values of lattice constants but also the temperature dependence. It is considered that larger FMR appears in KTN($x = 0.011$) at low temperature with the help of phonon softening. The experimental results thus obtained were compared with previous ones [3, 8]. Andrews [15] showed that both pure $KTaO_3$ and KTN($x = 0.017$) have the same lattice constants at room temperature within experimental errors. Both lattice constants have almost the same temperature change from room temperature to 200 K and each of them showed different temperature dependence below 200 K. We did not find such a behaviour in the temperature change of lattice constants for the three specimens. On the other hand, the similar experimental result between our results and Andrews's results is that pure $KTaO_3$ has no expansions of lattice constants at low-temperature and a small increase of lattice constants is seen in KTN($x = 0.017$). One of the reasons for these is the surface effect as Andrews pointed out [15], since the penetration depth of x-rays is so small. We have a plan to measure anisotropic HDS by the neutron diffraction method, since neutrons are more effective for oxygen distortion and the surface effect is ignored.

Acknowledgments

One of the authors (H Abe) acknowledges partial support at University of Houston from NSF-MRSEC and helpful discussion with Professor S C Moss.

References

[1] Vogt H 1995 *Phys. Rev.* B **51** 8046
[2] Uwe H 1985 *Japan. J. Appl. Phys.* **24** (suppl 2) 513
[3] Uwe H, Lyons K B, Carter H L and Fleury P A 1986 *Phys. Rev.* B **33** 6436
[4] Klink J J, Rod S and Chatelain A 1986 *Phys. Rev.* B **33** 2084
[5] Stachiotti M G and Migoni R L 1990 *J. Phys.: Condens. Matter* **2** 4341
[6] Rytz D, Hochli U T and Bilz H 1980 *Phys. Rev.* B **22** 359
[7] Rytz D and Scheel H J 1982 *J. Cryst. Growth* **59** 468
[8] Gehring P M, Chow H, Shapiro S M, Hriljac J A, Chen D H, Toulouse J, Rytz D and Boatner L A 1992 *Phys. Rev.* B **46** 5116
[9] Kleenman W, Schafer F J and Rytz D 1985 *Phys. Rev. Lett.* **54** 2038
[10] Ang C, Yu Z, Vilarinho P M and Baptista J L 1998 *Phys. Rev.* B **57** 7403
[11] Chou H, Shapiro S M, Lyons K B, Kejems J and Rytz D 1990 *Phys. Rev.* B **41** 7231
[12] Gehring P M, Chow H, Shapiro S M, Hriljac J A, Chen D H, Toulouse J, Rytz D and Boatner L A 1993 *Ferroelectrics* **150** 47
[13] Axe J D, Harada J and Shirane G 1970 *Phys. Rev.* B **1** 1227
[14] Comes R and Shirane G 1972 *Phys. Rev.* B **5** 1886
[15] Andrews S R 1985 *J. Phys. C: Solid State Phys.* **18** 1357
[16] Warren B E 1990 *X-Ray Diffraction* (New York: Dover)
[17] Wooster W A 1997 *Diffuse X-Ray Reflection from Crystals* (New York: Dover)
[18] Dederichs P H 1973 *J. Phys. F: Met. Phys.* **3** 471
[19] Barrett H H 1968 *Phys. Lett.* A **26** 217
[20] Perry C H, Currant R, Buhay H, Migoni R M, Stirling W G and Axe J D 1989 *Phys. Rev.* B **39** 8666
[21] *Landolt–Börnstein New Series* 1981 vol 16 (Berlin: Springer) p 408
[22] Eglitis R I, Kotomin E A, Borstel G and Dorfman S 1998 *J. Phys.: Condens. Matter* **10** 6271